



NASA Contractor Report 191413

ICASE Report No. 92-72

ICASE

**SIMULATION OF BOUNDARY-LAYER TRANSITION:
RECEPTIVITY TO SPIKE STAGE**

**Fabio P. Bertolotti
Jeffrey D. Crouch**

NASA Contract Nos. NAS1-18605 and NAS1-19480
December 1992

**DTIC
ELECTE
MAR 12 1993
S E D**

Institute for Computer Applications in Science and Engineering
NASA Langley Research Center
Hampton, Virginia 23681-0001

Operated by the Universities Space Research Association



National Aeronautics and
Space Administration

Langley Research Center
Hampton, Virginia 23681-0001

98 3 11 076

93-05246



208

DISTRIBUTION STATEMENT

Approved for public release
Distribution Unlimited

SIMULATION OF BOUNDARY-LAYER TRANSITION: RECEPTIVITY TO SPIKE STAGE

*Fabio P. Bertolotti*¹

Institute for Computer Applications in Science and Engineering
NASA Langley Research Center
Hampton, VA 23681-0001

and

*Jeffrey D. Crouch*²

Boeing Commercial Airplane Group
Seattle, WA 98124.

Accession For	
NTIS	CRA&I
DTIC	TAB
Unannounced	
Justification	
By	
Distribution /	
Availability Codes	
Dist	Avail and / or Special
A-1	

ABSTRACT

The transition to turbulence in a boundary layer over a flat plate with mild surface undulations is simulated using the parabolized stability equations (PSE). The simulations incorporate the receptivity, the linear growth, and the nonlinear interactions leading to breakdown. The nonlocalized receptivity couples acoustic perturbations in the free-stream with disturbances generated by the surface undulations to activate a resonance with the natural eigenmodes of the boundary layer. The nonlinear simulations display the influence of the receptivity inputs on transition. Results show the transition location to be highly sensitive to the amplitudes of both the acoustic disturbance and the surface waviness.

DTIC QUALITY INSPECTED 5

¹This research was supported by the National Aeronautics and Space Administration under NASA Contract Nos. NAS1-18605 and NAS1-19480 while the author was in residence at the Institute for Computer Applications in Science and Engineering (ICASE), NASA Langley Research Center, Hampton, VA 23681-0001. This author gratefully acknowledges the assistance and support provided by S.A. Orszag under DARPA contract N00014-86-K-0759 during the initial part of this work.

²Part of this work was conducted while this author was at the Naval Research Laboratory in Washington, DC, supported by an ONT Postdoctoral Fellowship.

I. Introduction

In the absence of significant cross flow or curvature, transition to turbulence generally results from the amplification of traveling eigenmodes such as Tollmien-Schlichting (TS) waves or Squires modes. These traveling modes are generated through the process called receptivity. While surface vibrations and atmospheric turbulence can activate receptivity mechanisms, experiments have shown that the laminar-turbulent transition over a wing surface is strongly affected by the acoustic field generated by the engines and the turbulent boundary layer on the fuselage [1].

The interaction of the acoustic field with a single bump has been the focus of several investigations in the past, e.g. Goldstein & Hultgren [2] and Kerschen [3]. These analyses are “decoupled” from the downstream disturbance evolutions, and are solved independently to provide the initial amplitudes for the evolution calculations. These and other receptivity studies have been primarily theoretical or experimental, but there are some ongoing studies based on numerical simulations, such as, for example, Lin, Reed & Saric’s [4] simulation of the receptivity to sound for a flat plate with a blunt leading edge.

A new mechanism has recently been forwarded by Crouch [5,6] based on small non-localized irregularities that cover the entire surface (e.g. undulations or roughness). Possible origins for these undulations include the extrusion and plate rolling process at the manufacturing stage, and heat and pressure induced distortions during flight. Unlike the localized case, the receptivity is mixed with the disturbance evolutions and both must be considered simultaneously. Studies indicate that, if operative, this mechanism is likely to dominate the receptivity process [7,8].

We employ the parabolized stability equations to simulate the boundary-layer transition over a wavy surface; we include both the receptivity and the subsequent linear and nonlinear evolutions. The relative efficiency of the PSE simulations accommodates the investigation of the effects of “receptivity input parameters” on the path to transition. These investigations display the strong effect which small, i.e. $\mathcal{O}(1)$, changes in the wall roughness height and geometry have on the transition process.

II. Wall geometry and acoustic field

We consider a flat plate immersed in an incompressible flow field with acoustic noise. The plate surface is covered by small amplitude irregularities with length scales comparable to TS waves.

We employ a Cartesian coordinate system with the average plate surface in the x^*-z^* plane, x^* measuring streamwise distance, and y^* the distance normal to the plate (the

symbol $*$ denotes a dimensional quantity). We nondimensionalize quantities using the free-stream velocity U_∞^* and the length $\delta_r^* = \sqrt{\nu^* x_r^* / U_\infty^*}$, with x_r^* being the location where the Reynolds number $R_x = U_\infty^* x_r^* / \nu^*$ equals one million. Results are presented in terms of the usual stability parameters, $R = \sqrt{R_x}$ (distance) and $F = 10^6 (\omega^* / 2\pi) \nu^* / (U_\infty^*)^2$ (frequency).

The x - z -periodic function $H(x, z)$ describes the surface undulations. We represent H by its Fourier series representation,

$$H(x, z) = \sum_{r=-\infty}^{\infty} \sum_{s=-\infty}^{\infty} \mathcal{W}_{r,s} e^{i r \alpha x} e^{i s \beta z} \quad (1)$$

where the coefficients $\mathcal{W}_{r,s}$ and $\mathcal{W}_{-r,-s}$ are complex conjugates. Additionally, we impose symmetry in z , thus $\mathcal{W}_{r,s} = \mathcal{W}_{r,-s}$. We use values of $|\mathcal{W}|$ of the order of 0.002 (see Table 1) which translate into a height to wavelength ratio of order 1/1000. At STP and $U_\infty^* = 10 \text{ m/s}$ the peak-to-peak surface variation is in the range of 30 micrometers, while at $U_\infty^* = 100 \text{ m/s}$ the variation is about 10 micrometers.

The free-stream acoustic field is of the form

$$u = \sum_{l=-\infty}^{\infty} \mathcal{A}_l e^{-il\omega t}, \quad v = w = 0. \quad (2)$$

Associated with each discrete acoustic frequency \mathcal{A}_l is a velocity field having a Stokes layer at the wall satisfying the no slip boundary condition, and matching the acoustic field in the free-stream. The values of ω in (2), and of α and β in (1) represent the lowest common divisor of the set of frequencies and wave numbers present. In case the wall spectrum is dominated by sharp peaks but the acoustic spectrum is not, we choose ω such that for each wall mode $(n\alpha, k\beta)$, the triplet $(l\omega, n\alpha, k\beta)$ is as close to branch I of the TS wave neutral stability curve as possible. In this way we focus our attention on the temporal-spatial combination that will feed the greatest amount of energy into the eigenmodes. Conversely, if a flat spatial spectrum is present and isolated peaks exist in the acoustic spectrum, we select the values of α and β that yield triplets close to branch I.

III. Receptivity mechanism

Acoustic disturbances in the free-stream generate Stokes modes within the boundary layer. In the incompressible limit these modes have only temporal modulation,

$$\mathbf{v}_l = \hat{\mathbf{v}}_l(y) e^{il\omega t} + c.c., \quad l = \dots, -2, -1, 1, 2, \dots \quad (3)$$

Meanwhile, the mean flow over a wavy surface produces steady wall modes,

$$\mathbf{v}_{n,k} = \hat{\mathbf{v}}_{n,k}(x, y) e^{in\alpha x + ik\beta z} + c.c.,$$

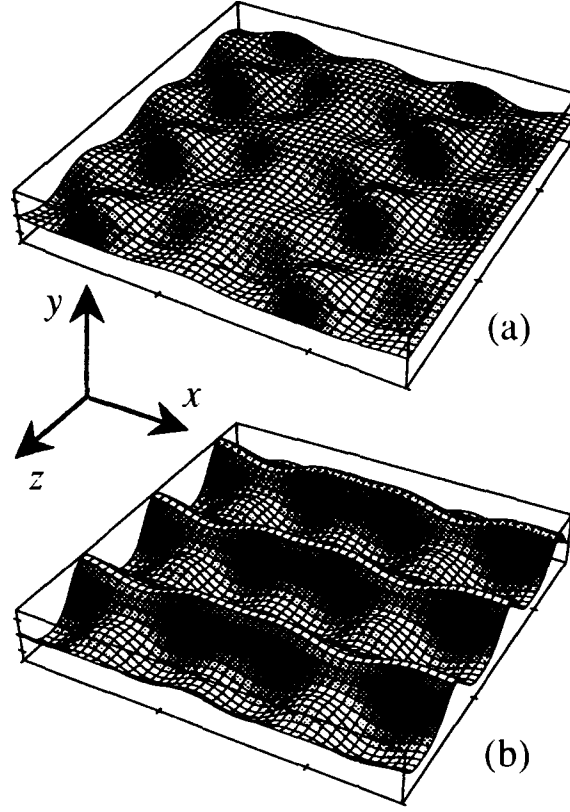


Figure 1: Rendition of surface undulations used in present study. The normal coordinate is stretched. (a) Case “high” and “low”, (b) Case “riblet”.

$$n, k = \dots, -2, -1, 1, 2, \dots \quad (4)$$

These modes are standing waves with wave numbers given directly by the surface. Single-handedly, neither the acoustic nor the wall velocity fields can directly energize a traveling eigenmode since these fields lack the necessary spatial or temporal variation, respectively. However, the simultaneous presence of both fields produces traveling waves due to the quadratic nonlinearity of the Navier-Stokes equations,

$$\mathbf{v}_{l,n,k} = \hat{\mathbf{v}}_{l,n,k}(x, y) e^{-il\omega t + ik\beta z + i\alpha_e x}, \quad (5)$$

whose form is identical to that of the natural eigenmode of the boundary layer, except the value of the exponent α may not match that of the eigenmode of the boundary layer stability equations, which has the form,

$$\mathbf{v}_{l,n,k} = \hat{\mathbf{v}}_{l,n,k}(x, y) e^{-il\omega t + ik\beta z + \int_{x_0}^x a_e(s) ds},$$

$$a_e = \gamma_e + i\alpha_e, \quad (6)$$

The receptivity mechanism is illustrated in Figure 2.

The key ingredient to the nonlocalized receptivity process is a resonance which results when the wall wave number α approaches the eigenmode wave number $a_e = \gamma_e + i\alpha_e$. Here, γ is the growth rate. Near branch I the growth rate is small, and, for an appropriate value of α , the difference $|a_e - \alpha|$ may be small. The resulting response of the boundary layer, under the forcing provided by the traveling wave may be quite large. The detuning $|a_e - \alpha|$

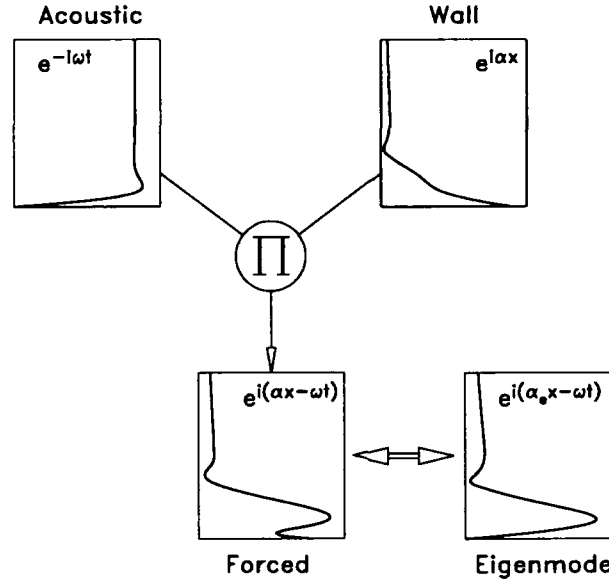


Figure 2: Components of the nonlocalized receptivity model (Spanwise wavenumber βz not shown).

changes as the modes are convected downstream. During the large response near branch I, energy is transferred into the eigenmode of the boundary layer. The nonlocalized receptivity model [5,7] shows that the rate of energy transfer between the forced wave and the eigenmode is proportional to the rate of variation of the forced wave response. Farther downstream, the eigenmode undergoes the typical exponential growth characteristic of the linear regime. Receptivity results from the net energy transfer into the eigenmode. The superposition of the forced wave and the eigenmode, with their appropriate wave numbers, provides the total (physical) traveling-wave disturbance.

IV. The PSE formulation

As a consequence of the basic flow being independent of the spanwise coordinate z , we can reduce the number of unknowns from velocity components u , v , w (along x , y , and z , respectively) and pressure p to only u and v . We eliminate pressure by taking the curl of the momentum equation, and w using the continuity equation. The boundary conditions are

zero velocity at the wall, and (except for the acoustic modes and the mean-flow distortion) vanishing velocity far from the plate.

The parabolized stability equations, commonly abbreviated to PSE, were developed by Herbert & Bertolotti [9] to incorporate nonlinearity and the slow growth of the boundary layer into the boundary-layer stability computations. The results were found to agree with those of full DNS simulations up to “spike stage”, where the complexity of the flow rapidly spreads beyond the resolution of the PSE code [10,11,12].

Herein we extend the PSE formulation to incorporate the nonlocalized receptivity model. We express the velocity field in a series in time (index l), in x (index n) and in z (index k),

$$\mathbf{v}(x, y, z, t) = \mathbf{V}_B(x, y) + \sum_{l=-\infty}^{\infty} \sum_{n=-\infty}^{\infty} \sum_{k=-\infty}^{\infty} \mathbf{v}_p(x, y, z, t) \quad (7)$$

where, \mathbf{p} is the wave-vector (l, n, k) . The velocity field of each mode is partitioned into

$$\mathbf{v}_p(x, y, z, t) = A_p(x) \hat{\mathbf{v}}_p(x, y) \chi_p(x, z, t). \quad (8)$$

The function

$$A_p(x) = \exp \left[\int_{x_0}^x \gamma_p(s) ds \right] \quad (9)$$

incorporates (in a sense made specific below) the amplitude of each mode and the function χ incorporates the wavelike part of the mode’s velocity field

$$\chi_p(x, z, t) = \exp [in\alpha x + ik\beta z - il\omega t]. \quad (10)$$

This formulation differs from the regular PSE formulation [12] in that the wavenumber α in (10) is not a function of x , but, rather, is held constant in order to accommodate the wall Fourier modes. As a consequence, the maximum allowable step-size yielding acceptable accuracy is significantly smaller than that permitted using the regular formulation. The reason for this reduction is that differences between the modes’ physical wavenumbers (based on u'_{max} , say) and the Fourier wavenumbers $n\alpha$ must be resolved by the profile functions $\hat{\mathbf{v}}_p$, which are subject to the “parabolization” approximation (12). We expand on this topic later on.

The acoustic and wall modes have a wave vector of the form, respectively,

$$\mathbf{p} = (\omega, 0, 0), (2\omega, 0, 0), \dots, (L\omega, 0, 0)$$

$$\mathbf{p} = (0, \alpha, 0), (0, 0, \beta), \dots, (0, N\alpha, K\beta).$$

Both the forced traveling wave, (5), and corresponding eigenmode, (6), have the same frequency and spanwise wave number, and *approximately* the same streamwise wave number.

Accordingly, both the forced and the eigenmode can be resolved by the Fourier mode having the wave vector

$$\mathbf{p} = (n\omega, n\alpha, k\beta)$$

for some n and k . In particular, the eigenmode wave number $n\alpha_e(x)$ varies with x and, hence will not equal the wall wavenumber $n\alpha$ except possibly at one point. The difference,

$$\Delta\chi_{\mathbf{p}} = e^{in \int_{x_0}^x (\alpha_e(s) - \alpha) ds} \quad (11)$$

is resolved by the profile function $\hat{\mathbf{v}}_{\mathbf{p}}$. Thus, the dependence of $\hat{\mathbf{v}}_{\mathbf{p}}$ on x in eq (4) is the key factor that allows the PSE to capture the nonlocalized receptivity mechanism.

The partial differential equation governing the velocity profiles $\hat{\mathbf{v}}_{\mathbf{p}}$ is obtained by substituting the expansion (3) into the Navier-Stokes equations. For the streamwise derivatives we make use of the slow change with x of the profiles and growth rates with the rule

$$\frac{\partial^m \mathbf{v}_{\mathbf{p}}}{\partial x^m} = A_{\mathbf{p}} \left[a_{\mathbf{p}}^m \hat{\mathbf{v}}_{\mathbf{p}} + m a_{\mathbf{p}}^{m-1} \frac{\partial \hat{\mathbf{v}}_{\mathbf{p}}}{\partial x} + \frac{m}{2} (m-1) a_{\mathbf{p}}^{m-2} \frac{da_{\mathbf{p}}}{dx} \hat{\mathbf{v}}_{\mathbf{p}} \right] \chi_{\mathbf{p}}, \quad (12)$$

where $a_{\mathbf{p}}(x) = \gamma_{\mathbf{p}}(x) + in\alpha$. For $m > 1$ the streamwise derivatives of the mean-flow \mathbf{V}_B are zero, in accordance with the boundary-layer approximation. Similarly, in (7) we drop second- and higher-order derivatives with respect to x of $\hat{\mathbf{v}}_{\mathbf{p}}$ and $a_{\mathbf{p}}$. Performing harmonic balance yields an infinite set of coupled partial differential equations of parabolic type in x of the form

$$\mathbf{L}\hat{\mathbf{v}}_{\mathbf{p}} + \mathbf{M}\frac{\partial \hat{\mathbf{v}}_{\mathbf{p}}}{\partial x} + \frac{da_{\mathbf{p}}}{dx}\mathbf{N}\hat{\mathbf{v}}_{\mathbf{p}} = \sum_{\mathbf{r}} \mathbf{Q}[\mathbf{v}_{\mathbf{r}}, \mathbf{v}_{\mathbf{p}-\mathbf{r}}], \quad (13)$$

where the operators $\mathbf{L}, \mathbf{M}, \mathbf{N}$ and \mathbf{Q} contain derivatives with respect to y only. The summation on the r.h.s. of (3) is truncated to some number (L, N, K) in the numerical computations. Due to the symmetry in z we only need to solve for modes with non-negative wave numbers in t , x , and z . Upstream traveling modes are not allowed.

A second, and closing, set of equations for the PSE is needed to define the values of $\gamma_{\mathbf{p}}$ as a function of x . These equations remove the ambiguity existing in (4) wherein both $\hat{\mathbf{v}}_{\mathbf{p}}$ and $A_{\mathbf{p}}$ depend on x . In the present work we use an integral norm (although other choices are possible)

$$\mathcal{R} \left\{ \int_0^\infty \hat{u}_{\mathbf{p}}^\dagger \frac{\partial \hat{u}_{\mathbf{p}}}{\partial x} dy \right\} = 0 \quad (14)$$

where \mathcal{R} denotes the real part, and \dagger denotes the complex conjugate. See references [10,11,12] for more details.

We transfer the zero-slip wall boundary condition to $y = 0$ via a Taylor series expansion about $y = 0$, and stop the expansion at terms linear in $|H|$ since this quantity is assumed

small, although including higher orders in $|H|$ can be done in a straight forward fashion. Performing harmonic balance yields the boundary conditions satisfied by $\hat{\mathbf{v}}_{\mathbf{p}}$ for each \mathbf{p} ,

$$\hat{\mathbf{v}}_{\mathbf{p}}(x, 0) = \frac{-1}{A_{\mathbf{p}}(x)} \left[\mathcal{W}_{\mathbf{p}} \frac{\partial \mathbf{V}_B(x, 0)}{\partial y} + \sum_{\mathbf{r}} \mathcal{W}_{\mathbf{p}-\mathbf{r}} \frac{\partial \hat{\mathbf{v}}_{\mathbf{r}}(x, 0)}{\partial y} A_{\mathbf{r}}(x) \right]. \quad (15)$$

The initial conditions for the PSE are obtained by means of a local procedure that is composed of a system of ordinary differential equations and, hence, is free from upstream influence, as described in [10,11,12]. Briefly, the local procedure is derived by expanding $\hat{\mathbf{v}}_{\mathbf{p}}(x, y)$ in a two-term Taylor series about the x location of interest, and collecting terms of order $\mathcal{O}(1)$ and $\mathcal{O}(\Delta x)$. To be consistent with the ordering of terms, the wavenumber α and frequency ω is assumed greater than order $\mathcal{O}(R^{-1})$. Consequently, modes having zero wavenumber and frequency, such as vortices and the mean-flow distortion, are initialized differently, as described below.

The *xPSE* transition analysis tool-kit has been employed for the computations. The partial differential equations, (13), are transformed into algebraic form by use of a multi-domain spectral collocation technique in y , and a finite difference discretization in x . Five domains are used in y , with limits at $[0, 4]$, $[4, 12]$, $[12, 24]$, $[24, 50]$, $[50, 100]$ and u and v are approximated by 17 and 19 Chebychev polynomials, respectively, in each domain. Asymptotic boundary conditions are imposed at $y = 100$. In particular, in the far-field the velocity fields decay exponentially in y with rate ζ is imposed, using $\zeta = \zeta_1$ or ζ_2 , which ever has a smaller real part,

$$\zeta_1 = \sqrt{(k\beta)^2 - a_{\mathbf{p}}^2}$$

$$\zeta_2 = \frac{R_o V_B}{2} - \sqrt{\frac{(R_o V_B)^2}{4} + R_o(a_{\mathbf{p}} - il\omega) + \zeta_1^2}.$$

During every streamwise step, the nonlinear algebraic system is solved iteratively by modifying the values of $\gamma_{\mathbf{p}}$ until the normalization conditions (9) are satisfied to a pre-determine level of accuracy.

A further element affecting accuracy is the presence of (11) in $\hat{\mathbf{v}}_{\mathbf{p}}$. For small amounts of separation $|\alpha_e - \alpha|$, the difference in wavenumber is well captured by the streamwise change of $\hat{\mathbf{v}}_{\mathbf{p}}$. For larger amounts, however, the PSE results loose accuracy. A more detail study of this issue, as well as the effect of step-size on accuracy, can be found in reference [14]. It suffices here to say that a difference in $|\alpha_e - \alpha|/\alpha < 0.1$, along with steps sizes $\Delta x < 5$, lead to acceptably small errors. Increasing the differences above 10% leads to an underestimate of the growth rates.

V. Results

The presentation of the results is divided into three sections. In the first one we look at the effect of roughness height on transition using the surface shown in Figure 1a. Then, to this surface we add a spanwise periodic array of “riblets” aligned with the streamwise direction, as shown in fig 1b, and show how their presence triggers transition. The initial conditions for the steady modes in the riblet case need special treatment, and a discussion is presented prior to the results. Afterwards, we investigate the effect of raising the acoustic level on the transition location. Even though we only carry a few modes and frequencies in our calculations, our results lie close to the experimental correlations between transition location and free-stream turbulence levels. All quantities presented herein have been nondimensionalized with δ_r^* and U_∞^* .

To specify the problem, we need to select the number of acoustic modes present, and their frequency. Arbitrarily, we choose the frequency $F = 56$ and its subharmonic, $F = 28$. The presence of the subharmonic is needed to generate the traveling wave which will undergo parametric resonance with the fundamental mode at some point downstream. Given these frequencies, we select the wavelength of the wall modes to maximize receptivity. We choose the fundamental wavenumber α for the Fourier decomposition of the wall undulations to be $\alpha = 0.0871$, so that the wall mode with wavenumber 2α will closely match wavenumber $\alpha_e = 0.1723$ at branch I for a TS wave of frequency $F = 56$. The fundamental spanwise wavenumber β is set to the value of 0.15, so that $\beta \approx 2\alpha$ and the associated K and H type secondary instabilities are nearly maximally amplified [13].

While our selection of wavelengths for the wall modes is arbitrary, we note that within the range of variations we are dealing with (i.e. 10 to 30 micrometers) most wing surfaces will contain a large selection of undulations with different wavelengths, amongst which our particular choices are likely to be present.

The spectrum in the numerical calculation is truncated to $L = 2$, $N = 2$, $K = 2$ in t , x , and z , except for the riblet case, where $K = 3$ is used. The integration is started at $R = 300$, which is sufficiently upstream to include any significant resonance prior to branch I ($R = 589$ at $F = 56$), and marched downstream with a constant step size of $\Delta x = 3.5$. While the triple Fourier sum allows for 27 distinct modes, many of these modes do not play an active role in the transition process and can be excluded from the calculation. For example, the modes having phase speeds of either $2c = 2\omega/\alpha$ or $c/2 = \omega/2\alpha$ remain at roughly constant amplitude levels throughout the computation, and their presence does not alter the results shown herein. Apparently, the phase speed difference prevents strong participation with the interactions propagating at the speed c . Also, our results show that the interactions between modes of equal phase speed, but different from c , do not result in rapid amplitude growth.

In our study we employ three different plate geometries, which we label “high”, “low” and “riblet”. The coefficients in (1) are real and have the following values,

Table 1

	high	low	riblet
$\mathcal{W}_{(2,0)}$	2.0×10^{-3}	1.0×10^{-3}	1.0×10^{-3}
$\mathcal{W}_{(1,1)}$	2.0×10^{-3}	1.0×10^{-3}	1.0×10^{-3}
$\mathcal{W}_{(2,1)}$	2.0×10^{-3}	1.0×10^{-3}	1.0×10^{-3}
$\mathcal{W}_{(0,1)}$	0.0	0.0	5.0×10^{-3}
$\mathcal{W}_{(0,2)}$	0.0	0.0	1.25×10^{-3}

The geometry between “high” and “low” differs only in the peak-to-peak variation of the undulations. The “riblet” geometry contains two additional modes which describe stream-wise aligned undulations, similar to the streamwise “riblets” used in turbulence drag reduction, only that our “riblets” are not sharp peaked, and have a very small height.

V.1. Effect of roughness height

To study the effect of surface roughness height on transition we consider the “high” and “low” geometries. The acoustic modes have a u peak-to peak variation of $0.0010 U_\infty$, (i.e. $\mathcal{A}_1 = \mathcal{A}_2 = 0.0005$ in equation 2) while the peak-to-peak variation of the wall modes (Table 1) differ amongst each other by at most a factor of 2, hence no bias exists towards one particular mode. This scenario contrasts that of ribbon-induced transition where a two-dimensional mode dominates in amplitude prior to the onset of secondary instability.

Figure 3 displays the amplitude evolution of modes in the “high” roughness case. The transition process follows the well known subharmonic route. We focus our attention on two modes; the two-dimensional mode (2,2,0), which develops into a TS wave, and the (1,1,1) mode, which develops into the subharmonic mode. Initially each mode is composed solely of a forced traveling wave. As the modes propagate downstream the nonlocalized receptivity process pumps energy into the eigenmodes. Consequently, the (2,2,0) and (1,1,1) modes are of nearly the same amplitude and exhibit similar growth rates during their early evolution. At $R = 589$, the (2,2,0) mode passes through branch I. The eigensolution component of the mode undergoes exponential growth, while the forced traveling wave diminishes downstream.

The development of the subharmonic mode, (1,1,1), can be analyzed in two parts, the first one at locations below, say $R = 1050$ (including the sharp dip in amplitude), and the second one for locations above $R = 1050$. The first part is dominated by the process of receptivity, while the second part is dominated by the parametric resonance with the (2,2,0) mode. The

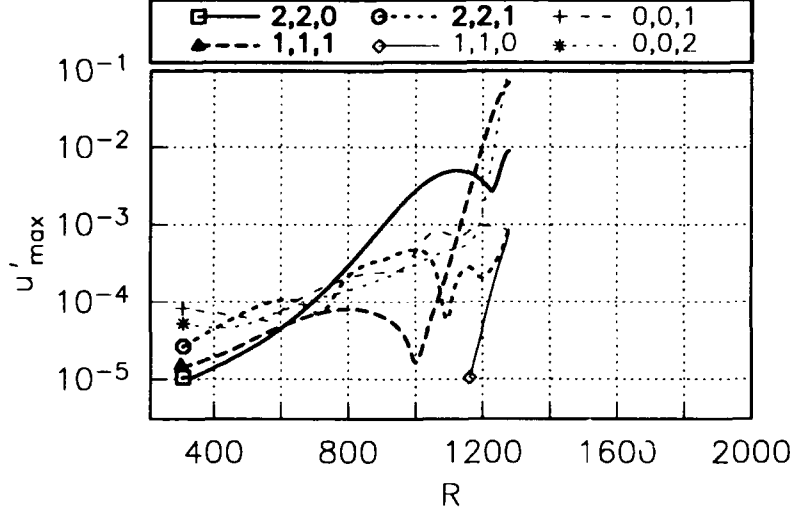


Figure 3: Root mean square of maximum u velocity versus R for the “high” roughness case.

dip in amplitude near $R = 1000$ is caused by a change in phase of 180 degrees in the complex velocity field $\hat{\mathbf{v}}_{(1,1,1)}$. This change is due to x dependent changes in the coefficients of the equations which govern the interaction between the forced mode and the eigenmode. At higher levels of acoustic forcing the receptivity and parametric regions overlap, eliminating this sharp dip in amplitude.

The (2,2,1) mode does not lead to fundamental (i.e. K-type) dynamics. The “porpoising” in amplitude seen in Figure 3 persists even with a four-fold increase in the acoustic amplitude, which increases by an equal amount the amplitude of the traveling modes, but only slightly the amplitude of the steady modes. The reason for this lack of K-type resonance, thus, cannot be explained simply in terms of a threshold amplitude of the (2,2,0) mode. Since K-type resonance involves the triad interaction between the (2,2,0), (2,2,1) and (0,0,1) modes, one may suspect an unfavorable phase relation in the triad to be quenching of the resonance. A four-fold increase in wall mode amplitudes, on the other hand, increases the amplitude of all modes, including the (0,0,1) mode, and the flow displays a mixed H-type and K-type transition.

Additional insight into the energy transfer between traveling modes and eigenmodes, as well as phase cancellation giving rise to the “porpoising” amplitudes, can be obtained from the perturbation theory [5] wherein the forced traveling wave and the eigensolution are kept distinct. In the PSE formulation one cannot easily separate the solution into the sum of the two components.

Lowering the amplitude of the wall undulations to the “low” level (see table 1) results in the dynamics shown in Figure 4. Between $R = 980$ and $R = 1200$ the subharmonic

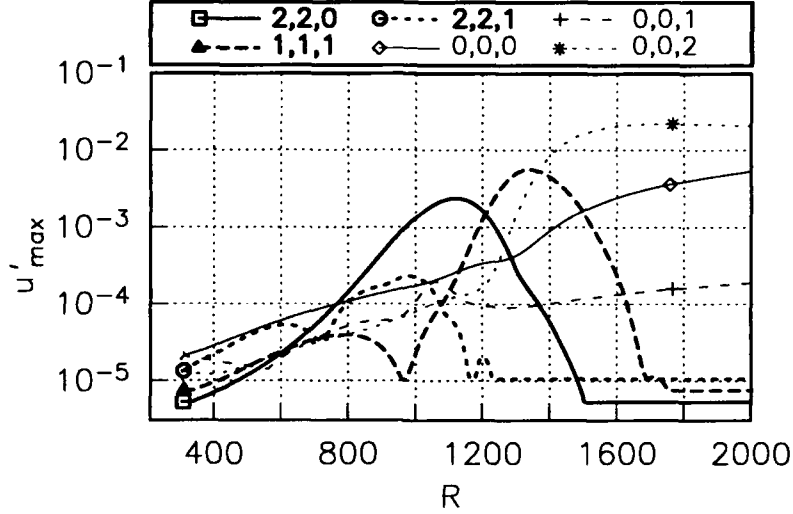


Figure 4: Root mean square of maximum u velocity versus R for the “low” roughness case.

undergoes rapid growth as in fig 3, however the amplitudes of the $(2,2,0)$ and $(1,1,1)$ modes remain below the threshold for self-sustained growth, causing these modes to decay after their respective branch II location at $R = 1116$ and $R = 1340$. The $(0,0,2)$ mode undergoes rapid growth past $R = 1200$ due to the direct forcing from the $(1,1,1)$ - $(1,1,1)$ interaction. Further downstream, this mode persists, albeit slowly decaying, being a remnant of the earlier parametric resonance. Similarly, the $(0,0,1)$ mode grows under the forcing from the $(2,2,0)$ - $(2,2,1)$ interaction. Both the mean-flow-distortion $(0,0,0)$ and this mode undergo weak algebraic growth past $R = 1400$ (see section V.2.1), but, eventually, the flow returns to its undisturbed state.

The results of the “high” and “low” roughness cases clearly display the sensitivity of the transition process on small changes of wall roughness height or, equivalently, on small variations of acoustic amplitude levels. This sensitivity highlights the difficulty of predicting transition with a simple criteria such as ϵ^n .

V.2. Effect of streamwise undulations

In the “high” roughness case, displayed in Figure 3, one can observe the birth of the mode $(1,1,0)$ at about $R = 1170$. This mode is of interest since as an eigenmode it has an unstable region that spans from $R = 864$ to $R \approx 2000$. This mode is forced via the $(0,0,1)$ - $(1,1,1)$ mode interaction, and since the wall Fourier mode $\mathcal{W}_{(0,1)}$ directly forces the mode $(0,0,1)$ through the wall boundary conditions, we looked into what effect a periodic array of streamwise “riblets” would have on transition. We represent these “riblets” with two Fourier modes with wavelength β and 2β . Consequently, our “riblets” are more blunt

and smaller than those used in turbulent drag reduction.

V.2.1. The initial condition

The generation of the initial conditions for the (0,0,1) and (0,0,2) modes at our starting location, $R = 300$ posed a problem. Several runs with the PSE showed that the evolution of this steady mode depends strongly on the initial conditions chosen. For some conditions, algebraic growth ensued. The dependence of the solution on the initial conditions persists far downstream, hence investigations are biased by the choice of initial conditions for the steady modes, or, equivalently, on the birth mechanism of these modes. Thus, we developed a particular, and reproducible, way of generating the initial conditions. Since large algebraic growth can obscure the dynamics of receptivity, and since the numerical initial conditions leading to such large growth may not be realizable in a real flow, we gauged the “correctness” of our initial conditions by the amount of algebraic growth present.

We generate the initial conditions by extending the riblets to the leading edge in such a way that a separation of variables approach is applicable with small error. The riblet is extended linearly from its full height at the PSE starting location, $x = x_0$, back to zero height at the leading edge, $x = 0$,

$$H(x, z) = \sum_{s=-2}^2 \left[\frac{x}{x_0} \mathcal{W}_{(0,s)} \right] e^{i s \beta z} \quad 0 \leq x \leq x_0$$

The wall forcing (15) involves the product of H with the derivative of the Blasius U component of velocity, which decreases as $x^{-1/2}$, therefore the forcing (15) increases as the \sqrt{x} over $0 < x < x_0$. Accordingly, in this x interval we introduce the following form for the (0,0,1) velocity field,

$$\begin{aligned} u(x, y, z) &= \hat{u}(y) \sqrt{\frac{x}{x_0}} e^{-i\beta z} \\ v(x, y, z) &= \hat{v}(y) \frac{1}{x_0} \sqrt{\frac{x}{x_0}} e^{-i\beta z} \\ w(x, y, z) &= \hat{w}(y) \frac{1}{x_0} \sqrt{\frac{x}{x_0}} e^{-i\beta z}, \end{aligned}$$

with a similar form for the (0,0,2) field. The boundary conditions reduce to an x independent form,

$$\hat{u}(0) = -\mathcal{W}_{0,1} f''(0), \quad \hat{v}(0) = 0, \quad \hat{w}(0) = 0$$

where f is the self-similar stream function of Blasius. The continuity and momentum equations contain coefficients that depend on x , so the separation of variables technique is not

strictly valid. However, the variation with x is slow enough to be negligible. For example, expanding $x = x_0 + \Delta x$, the continuity equation reduces to,

$$\hat{u} + 2\frac{d\hat{v}}{dy} + 2\frac{i\beta}{x_0}\hat{w} = \frac{\Delta x}{x_0 + \Delta x}\hat{u}$$

The right-hand-side depends on x but is $\mathcal{O}(R_0^{-1})$ near $x = x_0$. We set the right-hand-side to zero and solve the equations at $x = x_0 = 300$. The downstream evolution of the (0,0,1)

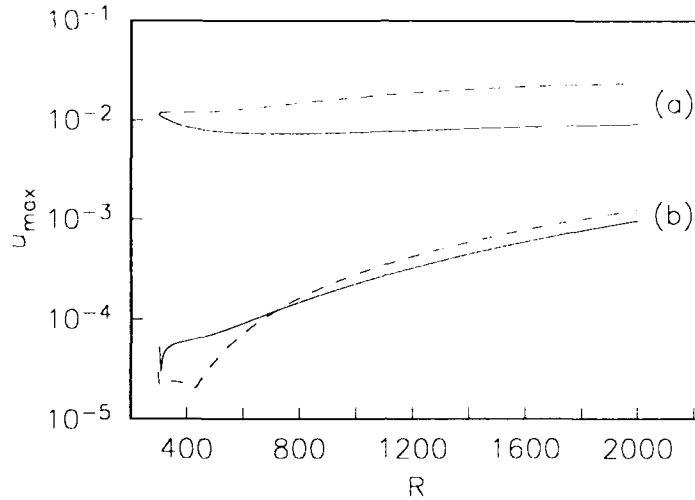


Figure 5: Amplitude evolution of the (0,0,1) mode, (a), and of the (0,0,0) mode, (b). Dashed lines show cases of algebraic growth.

mode is shown as the solid line associated with label “(a)” in Figure 5. The amplitude remains nearly constant over the domain of integration, showing only a weak transient near $R_0 = 300$. Negligible algebraic growth is present, and, in this respect, our initial conditions successfully generate a quasi-uniform downstream solution. In contrast, the dashed line associated with label “(a)” corresponds to a (0,0,1) mode generated via the local procedure, and displays the linear growth (when plotted in x vs. A) characteristic of algebraic growth [15,16].

The mean-flow-distortion, i.e. mode (0,0,0), is started from zero, and also displays algebraic growth. The solid line associated with label “(b)” shows the development of the mean-flow-distortion in the presence of the (0,0,1) mode. The growth exhibited is, however, due mostly to algebraic growth. This fact can be deduced by overlaying on the Figure the evolution of the mean-flow-distortion that has had the (0,0,1) forcing removed after a few marching steps (shown as the dashed line).

V.2.2. Effect of riblets on transition

The addition of riblets to the “low” roughness case causes the flow to reach the later stages of transition. The amplitude evolution of selected modes is shown in Figure 6. In comparison with Figure 5, the $(0,0,1)$ mode has a much higher amplitude, and the $(1,1,1)$ - $(0,0,1)$ forcing generates the $(1,1,0)$ mode at about $R = 1100$. While initially driven mainly by the forcing, the eigenmode component of $(1,1,0)$ undergoes exponential growth (Branch I is at $R = 864$) and becomes the dominant component past $R = 1450$. Since at this frequency the eigenmode’s total amplification A_{II}/A_I is 7208, the $(1,1,0)$ mode grows sufficiently to produce a significant back-forcing on the $(1,1,1)$ mode via the $(1,1,0)$ - $(0,0,1)$ interaction.

Past $R = 1650$ the $(1,1,0)$, $(0,0,1)$ and $(1,1,1)$ modes behave like in the vortex-wave interaction study presented in [10], wherein these modes eventually lock into a K-type parametric resonance. A similar triad resonance develops between the $(1,1,0)$, $(0,0,2)$, and $(1,1,2)$ modes. The flow at $R = 1970$ reaches a strongly nonlinear stage which precedes the onset of turbulence.

We like to refer to the evolution shown in Figure 6 as the “lateral”, since the first strong interaction of H-type sets the stage for the following K-type. This progression from higher to lower frequencies follows the slope of the branch I of the neutral stability curve as the Reynolds number increases, and thus, maintains the dominant modes near, or inside, the eigenmode’s region of instability.

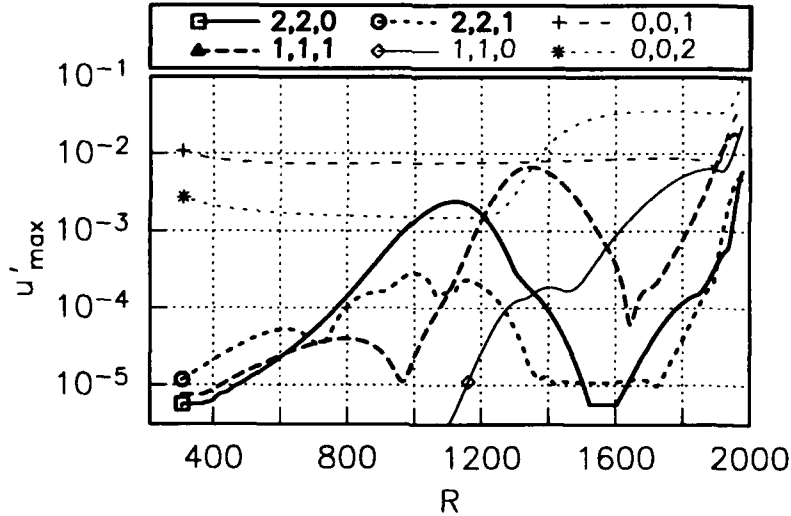


Figure 6: Root mean square of maximum u velocity versus R for the “Riblet” roughness case.

Figure 7 gives a visual synopsis of the “riblet” results. Shown as a solid line and a dashed line, respectively, are the neutral stability curves of two-dimensional and three-dimensional

disturbances given by the linearized stability equations. Superimposed are four constant frequency bands that represent four particular modes present in our calculation. The bands display, roughly, the location and extent of the receptivity (light gray), linear stage (white) and nonlinear stage (dark gray) in our computational domain. The upper of the two bands at $F = 56$ corresponds to the (2,2,0) mode, and the one just below it corresponds to the (2,2,1) mode. Similarly, the two bands at $F = 28$ correspond to the (1,1,0) mode (above) and the (1,1,1) mode (below). The band at $F = 0$ represents the (0,0,2) mode. For this mode the receptivity region denotes the direct forcing by the $\mathcal{W}_{(0,2)}$ wall mode.

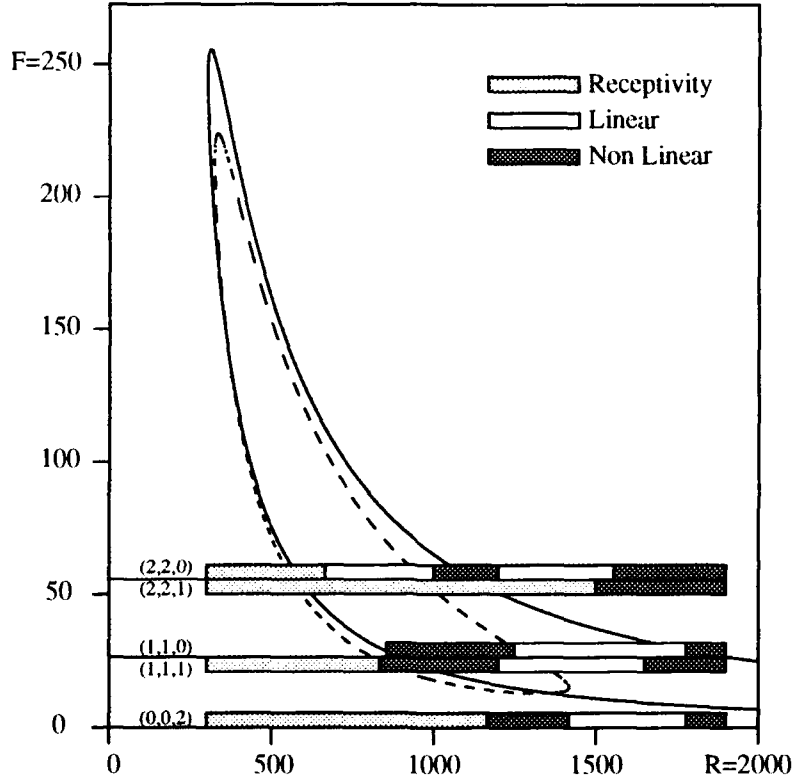


Figure 7: Visual synopsis of the dynamics shown in figure 6. Integer triplets denote the mode represented by each strip.

V.3 Effect of acoustic levels on R_{trans}

We close this section with the results of our investigation into the effect of the acoustic forcing level on the transition Reynolds number. While keeping the wall geometry fixed (“high” case), we increased the acoustic amplitude levels of both frequency components $F = 56$ and $F = 28$ from $\mathcal{A}_l = 0.0005$ used in our studies above, to $\mathcal{A}_l = 0.002$, 0.01 , and 0.02 . The corresponding r.m.s. amplitude levels are $\sqrt{2}$ times larger. Since our simulations do not reach into the turbulent flow regime, we arbitrarily defined the transition Reynolds

number as the location where the subharmonic mode reaches 6% amplitude. At this point the flow is engaged in the strong nonlinear interaction characteristic of spike stage, and the turbulent regime usually follows within a couple of streamwise wavelengths, $2\pi/\alpha$. We

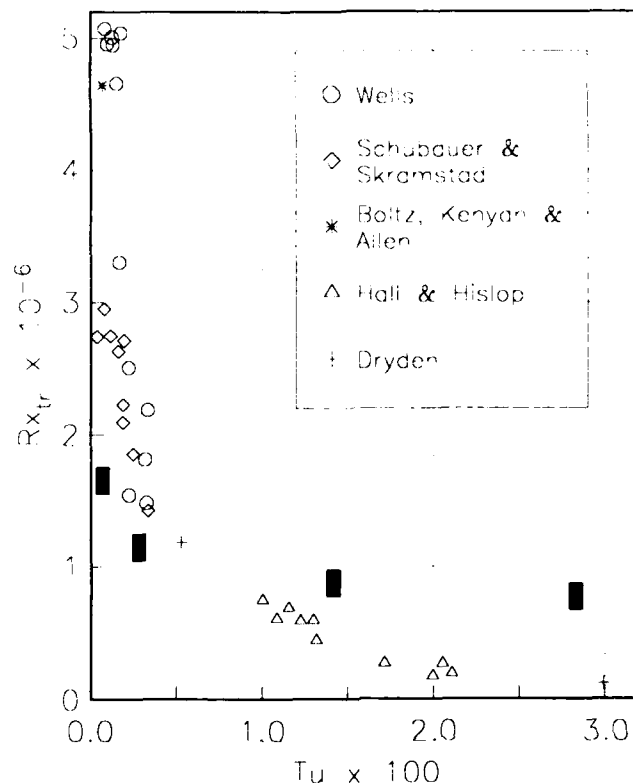


Figure 8: Transition R_x versus free-stream turbulence level, Tu . Dark bands represent computed results.

compare our results with the summary of experimental data presented by Arnal in [1]. The experimentally measured (free-stream) turbulence level was based on the r.m.s. fluctuation of all three velocity components, and even though this quantity consisted of a mixture of both sound and vorticity, our data matches qualitatively with the experimental ones, as shown in Figure 8 (note that $R^2 = R_x$). The higher numbers of $R_{x_{tr}}$ experimentally measured at the quiet limit suggest that a wall smoother than the one modeled here was used in the wind-tunnel tests, while the lower $R_{x_{tr}}$ measured at higher free-stream turbulence levels suggest that other mechanisms in addition to those considered herein are at work. Considering the simplicity of our model, the “ball-park” agreement of results is surprising.

VI. Conclusion

Given the description of the acoustic field spectrum and of the wavy wall geometry, we have followed the boundary layer response through the regions of receptivity, linear growth, and nonlinear mode interaction. The “bareness” of the input data needed for the numerical computation, namely the $\mathcal{W}_{(n,k)}$ and \mathcal{A}_l coefficients in equations (1) and (2), along with the efficiency inherent to the marching procedure, facilitates the exploration into the effects of receptivity parameters on transition. Here we have varied (slightly) the amplitude of the surface undulations to show two different downstream evolutions, one of which reaches spike stage, the other one returning to the Blasius profile. Adding streamwise riblets to the later case brings about spike stage through a “lateral” mechanism involving the transfer of resonance from higher frequencies to lower ones. Our results on the effect of acoustic amplitude level on the transition location compare qualitatively with wind tunnel measurements involving free-stream turbulence, despite the simplicity of our model. Both the acoustic level used (0.007% U_∞ , r.m.s) and amplitudes of the surface waviness ($30\mu m$, or less) make our investigation relevant to flight conditions.

References

- [1] D. Arnal, “Boundary Layer Transition: Prediction, Application to Drag Reduction,” AGARD Report 786 (Skin friction drag reduction), VKI, Brussels, 1992.
- [2] M.E. Goldstein and L.S. Hultgren, *Ann. Rev. Fluid Mech.*, **21** (1989) pp. 137-166.
- [3] E.J. Kerschen, AIAA Paper 89-1109 (1989).
- [4] N. Lin, H.L. Reed and W.S. Saric, *Bull. Am. Phys. Soc.*, **35** (1990) p. 2260.
- [5] J.D. Crouch, “Non-localized receptivity of boundary layers,” *J. Fluid Mech.*, **244**, pp. 567-581, (1992).
- [6] J.D. Crouch, *Bull. Am. Phys. Soc.*, **35** (1990) p. 2262.
- [7] J.D. Crouch, *Boundary Layer Stability and Transition to Turbulence*, ASME FED-Vol. **114** (1991) pp. 63-68.
- [8] J.D. Crouch and F.P. Bertolotti, AIAA Paper 92-0740 (1992).
- [9] Th. Herbert and F.P. Bertolotti, *Bull. Am. Phys. Soc.*, **32** (1987) p. 2079.

- [10] F.P. Bertolotti, *Linear and Nonlinear Stability of Boundary Layers with Streamwise Varying Properties*, PhD Thesis, The Ohio State University (1991).
- [11] Th. Herbert, AIAA Paper 91-0737 (1991).
- [12] F.P. Bertolotti, Th. Herbert and P.R. Spalart, "Linear and nonlinear stability of the Blasius boundary layer," J. Fluid Mech., **242**, pp. 441-474, (1992).
- [13] Th. Herbert, "Secondary instability of boundary layers," Ann. Rev. Fluid Mech., **20** (1988) pp. 487-526.
- [14] F.P. Bertolotti and J.D. Crouch, "Simulation of boundary-layer transition: receptivity to spike stage," Proc. First Euro. Comp. Fluid Dynam. Conference, Brussels, Belgium, Sept. 1992, pp. 183-190. Elsevier Science Publishers B.V.
- [15] P.J. Schmid and D.S. Henningson, "A new mechanism for rapid transition involving a pair of oblique waves," Phys. Fluids A., to appear, (1992).
- [16] S.C. Reddy and D.S. Henningson, "Energy growth in viscous channel flows," J. Fluid Mech., submitted, (1992).

REPORT DOCUMENTATION PAGE			Form Approved OMB No 0704-0188	
<small>Public reporting burden for this collection of information is estimated to average 1 hour per response, including the time for reviewing instructions, searching existing data sources, gathering and maintaining the data needed, and completing and reviewing the collection of information. Send comments regarding this burden estimate or any other aspect of this collection of information, including suggestions for reducing this burden, to Washington Headquarters Services, Directorate for Information Operations and Reports, 1215 Jefferson Davis Highway, Suite 1204, Arlington, VA 22202-4302, and to the Office of Management and Budget, Paperwork Reduction Project (0704-0188), Washington, DC 20503.</small>				
1. AGENCY USE ONLY (Leave blank)	2. REPORT DATE December 1992	3. REPORT TYPE AND DATES COVERED Contractor Report		
4. TITLE AND SUBTITLE SIMULATION OF BOUNDARY-LAYER TRANSITION: RECEPTIVITY TO SPIKE STAGE		5. FUNDING NUMBERS C NAS1-18605 C NAS1-19480 WU 505-90-52-01		
6. AUTHOR(S) Fabio P. Bertolotti Jeffrey D. Crouch				
7. PERFORMING ORGANIZATION NAME(S) AND ADDRESS(ES) Institute for Computer Applications in Science and Engineering Mail Stop 132C, NASA Langley Research Center Hampton, VA 23681-0001		8. PERFORMING ORGANIZATION REPORT NUMBER ICASE Report No. 92-72		
9. SPONSORING/MONITORING AGENCY NAME(S) AND ADDRESS(ES) National Aeronautics and Space Administration Langley Research Center Hampton, VA 23681-0001		10. SPONSORING/MONITORING AGENCY REPORT NUMBER NASA CR-191413 ICASE Report No. 92-72		
11. SUPPLEMENTARY NOTES Langley Technical Monitor: Michael F. Card Final Report To be submitted to Physics of Fluids				
12a. DISTRIBUTION/AVAILABILITY STATEMENT Unclassified - Unlimited Subject Category 34		12b. DISTRIBUTION CODE		
13. ABSTRACT (Maximum 200 words) The transition to turbulence in a boundary layer over a flat plate with mild surface undulations is simulated using the parabolized stability equations (PSE). The simulations incorporate the receptivity; the linear growth, and the nonlinear interactions leading to breakdown. The nonlocalized receptivity couples acoustic perturbations in the free stream with disturbances generated by the surface undulations to activate a resonance with the natural eigenmodes of the boundary layer. The nonlinear simulations display the influence of the receptivity inputs on transition. Results show the transition location to be highly sensitive to the amplitudes of both the acoustic disturbance and the surface waviness.				
14. SUBJECT TERMS receptivity; laminar to turbulence transition; boundary layer			15. NUMBER OF PAGES 20	
			16. PRICE CODE A03	
17. SECURITY CLASSIFICATION OF REPORT Unclassified	18. SECURITY CLASSIFICATION OF THIS PAGE Unclassified	19. SECURITY CLASSIFICATION OF ABSTRACT	20. LIMITATION OF ABSTRACT	